# Temperature dependence of Raman scattering in CdO: Insights into phonon anharmonicity and plasmon excitations

Ramon Cuscó

*GEO3BCN-CSIC, Consejo Superior de Investigaciones Científicas,*

*Lluís Solé i Sabarís s.n., 08028 Barcelona, Spain*

Javier Yeste and Vicente Muñoz-Sanjosé

*Dept. Física Aplicada i Electromagnetisme, Universitat de València,*

*Dr. Moliner 50, València, 46100 Burjasot, Spain*

## Abstract

We present a temperature-dependent Raman scattering study of CdO in the temperature range between 80 and 500 K. Distinctive features present in the second-order Raman spectra of CdO are identified as overtones and combinations modes with the help of density functional perturbation theory calculations. A wide broad band in the region between 250 and 470 $cm^{-1}$ is attributed to Raman scattering by charge-density fluctuations in the high-density overdamped electron gas present in the sample. A very good agreement is found between the Raman spectra and the expected scattering arising from the overtone density of states and plasmon excitations. The temperature dependence of the modes yields information about the anharmonic phonon interactions. Four-phonon processes arising from quartic anharmonicity play a significant role in the observed temperature dependence.

PACS numbers: 78.30.-j,63.20.Ry

## I. INTRODUCTION

Recently, there has been a growing interest in the family of binary oxides owing to their promising functional properties in a wide range of important technological applications [1]. CdO belongs to the family of rock-salt structured binary oxides and it has attracted attention as a thin-film transparent conductor [2], thermoelectric material [3], and more recently, as a promising emerging material for plasmonics [4–7]. CdO may also have an impact on widening the possibilities of two dimensional layered materials, as oxide materials containing *d* orbitals such as CdO and HfO have been predicted to form graphene-like monolayers with high stability [8].

Accurate knowledge of the basic physical properties of CdO is relevant for these applications. There exists some dispersion in the values reported in the literature, probably owing to different crystal quality and the presence of a high free carrier density due to oxygen vacancies. For instance, the direct band gap was determined to be 2.28 eV from 100 K thermoreflectance measurements [9]. Detailed analysis of infrared reflectivity, absorption and Hall effect measurements of high quality single crystal epitaxial layers, taking into account band nonparabolicity, band filling and band-gap renormalization, yielded a band gap of 2.16 eV [6]. Thermal conductivity has also been revisited, and one order of magnitude increase relative to previous reported values has been proposed in the light of first-principle calculations and recent experiments [10].

Optical characterization by means of Raman scattering is severely limited in rock-salt structured materials because first-order Raman scattering is symmetry forbidden. The fact that every atom of the lattice is a center of inversion imposes that the third-rank Raman tensor (the derivative of the polarizability tensor with respect the phonon coordinate) is identically zero. The first Raman scattering measurements of CdO were performed on polycrystalline samples and revealed only weak second-order Raman spectra [11], as already observed previously in a series of measurements on rock-salt structured alkali halides [12]. Today, high-quality fully relaxed CdO layers can be grown directly on *r*-plane sapphire by metal-organic chemical vapor deposition (MOCVD) [13]. A preliminary study of the improved quality Raman spectra of these single-crystal epitaxial layers was reported [14]. Some features were tentatively assigned based on *ab-initio* phonon calculations [14], although the calculated phonon frequencies appeared to be significantly underestimated. The behavior of the second-order Raman spectrum was

further investigated under high pressures [15].

In this work, we present a thorough Raman investigation of CdO, where the most distinctive features of the second-order Raman spectrum are identified with the aid of density functional perturbation theory (DFPT) calculations. The overall shape of spectrum, which displays a intense, wide central band, is addressed, as well as the temperature dependence of the most salient features of the spectrum. Detailed calculations of scattering by excitations of the high-density overdamped plasma and a semiempirical perturbative approach to phonon anharmonic decay provide a comprehensive description of the second-order Raman spectrum of CdO and its temperature dependence. Information about the acoustic phonon lifetimes is extracted from the temperature dependence of the second-order Raman peaks. A good knowledge of acoustic phonon lifetimes is of great interest for the analysis of the thermal conductivity of the materials [16].

## II. EXPERIMENT

Single crystal CdO epilayer with thickness ~ 500 nm were grown by metal-organic vapor-phase epitaxy (MOCVD) on *r*-plane sapphire substrates. Tertiary butanol and dimethylcadmium were used as precursors in a a reactor equipped with two independent gas inlets. The sample was kept at 304 °C on a radio-frequency heated graphite susceptor. Details of the sample growth and structural characterization are given elsewhere [13].

Raman scattering spectra were excited with the 488-nm line of an $Ar^+$ laser in backscattering from a *c* face and analyzed using a Jobin-Yvon T64000 spectrometer equipped with a liquid $N_2$ ($LN_2$) cooled charge-coupled detector (CCD). The measurements in the temperature range between 80 and 350 K were performed using a TBT-AirLiquide $LN_2$ cryostat equipped with a platinum resistance sensor and a temperature controller. Measurements at higher temperatures up to 500 K were carried out using a Linkam THMS600 heating stage.

DFPT calculations were performed in the framework of local density approximation (LDA). The projector augmented wave (PAW) approach as implemented in the ABINIT package [17] was employed, with datasets derived from ultrasoft potentials [18]. The dynamical matrix was obtained on a mesh of $k$ points using perturbation-theory linear-response and interpolated to arbitrary wave vectors for the calculation of phonon dispersion and density of states. An energy cutoff of 50 hartree and a $8 \times 8 \times 8$ Monkhorst-Pack $k$-point sampling were used in the calculations.

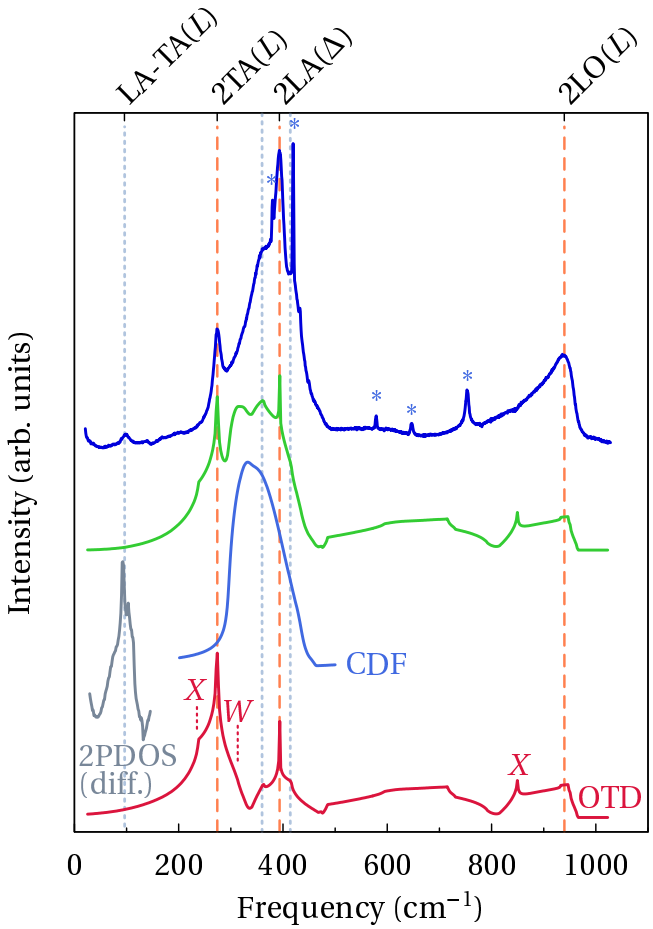


FIG. 1. Second-order Raman spectrum of the CdO film at 80 K (top blue line), compared to the distribution of phonon overtones (OTD) obtained from density functional perturbation theory calculations (bottom red line). A smooth scaling of the frequency axis in the OTD has been performed to bring the sharp distinctive features in perfect match with the Raman spectrum (highlighted by dashed orange lines). Raman peaks arising from the sapphire substrate are marked with asterisks. The contribution of charge-density fluctuations is depicted by the light blue trace labeled CDF. The sum of the ODT and CDF contributions is plotted as a green line. The scaled two-phonon difference density of states in the LA-TA($L$) spectral region is also shown as a grey line.

## III. RESULTS AND DISCUSSION

### A. The second-order Raman spectrum of CdO

The Raman spectrum of the CdO sample at 80 K is shown in Fig. 1 (top blue curve). Although the excitation energy used (2.54 eV) was above the nominal band-gap energy of CdO

(~ 2.2 eV), the absorption edge in our samples is shifted to higher energies due to band filling effects (Burstein-Moss shift). As a result, several Raman peaks arising from the sapphire substrate can still be seen, which are marked with asterisks. Besides a prominent central band between 250 and 480 $cm^{-1}$, several narrow peaks are observed, which are related with critical points in the phonon dispersion where the phonon bands are notably flat and lead to a high phonon density of states (PDOS). Second-order scattering in CdO involves the generation of two phonons $(\omega_i, \mathbf{q}_i)$ and $(\omega_j, \mathbf{q}_j)$ by the electron-phonon interaction. For Stokes scattering, wave-vector conservation implies that $\mathbf{q}_i \approx -\mathbf{q}_j$, whereas $\mathbf{q}_i \approx \mathbf{q}_j$ for difference scattering. Since the tensors belonging to the identity representation ($A_{1g}$) produce the highest scattering efficiencies and $A_{1g}$ is contained in the product representation of overtones, the polarized second-order Raman spectrum should largely be an overtone spectrum [19].

### B. Phonon overtone distribution

For the interpretation and correct assignment of the features observed in the second-order spectra, reliable calculations of the phonon dispersion and the PDOS are crucial. Early works lacked such theoretical support and assignments were made by analogy with other compounds [11]. In a previous publication, we tentatively assigned the observed peaks based on *ab-initio* calculations of the phonon dispersion [14]. Unfortunately, the DFPT method in the local density approximation (LDA) or generalized gradient approximation (GGA) has intrinsic limitations associated with the accurate treatment of the localization of semicore $d$ electrons. It was found that phonon energies were systematically underestimated by norm-conserving Troullier-Martins pseudopotentials, by as much as ~ 40 $cm^{-1}$ in the case of the LO mode [14]. Here we have repeated the calculations using the PAW formalism using datasets from the new GBRV library [20] generated from ultrasoft pseudopotentials [18], at higher cutoff energies and $k$-sampling densities, but the phonon frequencies are only marginally improved (the LO mode is underestimated by 30 $cm^{-1}$). Nevertheless, the shape of the calculated PDOS bears an obvious resemblance to the measured spectrum, which suggests that the overall phonon structure is well reproduced by the calculations.

As discussed above, we expect the second-order Raman spectrum to reflect the overtone distribution according to [19, 21]

$$I_2(\omega) \propto [n_{\mathrm{BE}}(\omega/2, T) + 1]^2 \rho_{\mathrm{ph}}(\omega/2), \tag{1}$$

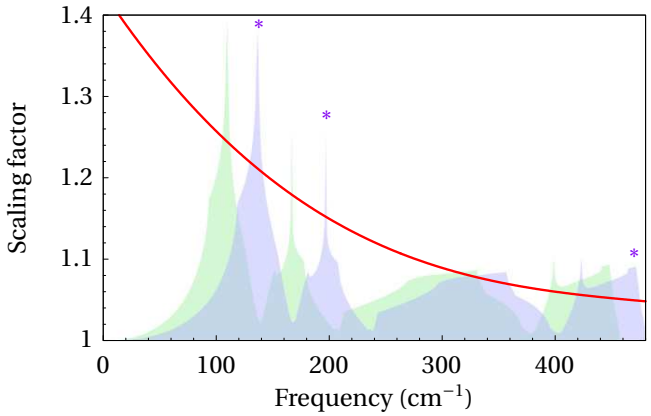


FIG. 2. Frequency-scaling function that brings the calculated PDOS into accord with the most prominent features of the second-order Raman spectrum (see text). The green and purple shaded areas correspond, respectively, to the PDOS before and after frequency scaling. The reference frequencies are marked with asterisks.

where $n_{\mathrm{BE}}(\omega, T)$ is the Bose-Einstein distribution and $\rho_{\mathrm{ph}}$ is PDOS. In the following discussions, we will use a modified phonon dispersion in which we have carried out a smooth continuous scaling of the energy axis to bring the most salient critical-point features, namely the calculated $\rho_{\mathrm{ph}}$ peaks at 111, 168, and 445 cm$^{-1}$, to coincide with the frequency of the second-order Raman peaks halved. A third-degree Chebyshev polynomial expansion with coefficients $a_0 = 1.428$, $a_1 = -2.08\times10^{-3}$ cm, $a_2 = 1.99\times10^{-6}$ cm$^2$, and $a_3 = -6.73\times10^{-10}$ cm$^3$ was employed as frequency-scaling function. The scaling function and the corresponding shift in the PDOS are shown in Fig. 2. The scaled overtone distribution (OTD) [Eq. (1)] is displayed in Fig. 1, where the alignment of the features used for the scaling is highlighted by the orange dashed lines. It is worth mentioning that other minor features also become aligned with the experimental spectrum, as depicted by the gray dotted lines. Most notably, a very good agreement is observed between the weak Raman peak at $\sim 98$ cm$^{-1}$ and the peak in the two-phonon difference density of states (2PDOS), displayed as a gray trace in Fig.1. All these observations strongly suggest that the scaled phonon dispersion may provide a more faithful description of phonons in CdO.

Notwithstanding the excellent agreement between the main critical points and the narrow peaks of the Raman spectrum, the latter displays an intense wide central band between 250 and 470 cm$^{-1}$ that is not reflected in the OTD. This central band had been attributed to first-order Raman scattering induced by oxygen deficiencies in CdO [11]. However, this is unlikely since there is no prominent structure in this spectral region in the PDOS. We address the origin of the

central band in the next section.

### C. Raman scattering by damped plasmon excitations

CdO samples display a high unintentional $n$-type conductivity originating in doubly ionized oxygen vacancies [4, 6]. The presence of a high-density free-electron plasma may give rise to Raman scattering by plasmon excitations. In fact, a broad Raman feature spanning a spectral region between TO and LO frequencies was reported on an overdamped plasma in cubic $n$-type GaN, and attributed to the charge-density-fluctuation mechanism [22].

MOCVD-grown CdO epitaxial layers typically exhibit electron densities $N_e \sim 1.5\times10^{20}$ cm$^{-3}$ and Hall mobilities $\mu \sim 83$ cm$^2$ V$^{-1}$ s$^{-1}$ [6, 23]. We take into account conduction band non-parabolicity via a two-band $\mathbf{k}\cdot\mathbf{p}$ Kane model [24]

$$E(k) = \frac{E_G}{2}\left[\sqrt{1+\frac{4}{E_G}\frac{\hbar^2k^2}{2m^*}}-1\right], \tag{2}$$

where $E_G$ is the band gap and $m^*$ is the band edge electron effective mass. We take the values $E_G = 2.16$ eV and $m^* = 0.21m_e$ from Ref. [6]. Using Eq. (2), for $N_e = 1.5\times10^{20}$ cm$^{-3}$ at 80 K, we find a Fermi wave vector of $k_F = 1.64\times10^7$ cm$^{-1}$ and a Thomas-Fermi screening wave vector of $q_{TF} = 1.37\times10^7$ cm$^{-1}$. At such high densities, the single particle regime (Landau damping region) for the plasmon excitations, $\hbar\omega_p(q) = E(k_F \pm q) - E(k_F)$, sets in very quickly and extends beyond $q_{TF}$ (see Fig. 3). Under wave-vector nonconservation induced by the charged impurities, large wave vectors contribute to scattering and the Raman line shape can be expressed as [25]

$$I(\omega) = \int_0^{q_{max}} dqF(q)\mathscr{L}(q,\omega), \tag{3}$$

where $\mathscr{L}(q,\omega)$ is the spectral line shape at wave vector $q$, and $F(q) = (4\pi)^2/(q^2+q_{TF}^2)$ is the Fourier transform of a Yukawa-type distribution. For the charge-density-fluctuation mechanism, the spectral line shape is given by [26]

$$\mathscr{L}(q,\omega) = q^2\left(\frac{\omega_{LO}^2-\omega^2}{\omega_{TO}^2-\omega^2}\right)^2 \mathrm{Im}\left\{\frac{-1}{\varepsilon(q,\omega)}\right\}. \tag{4}$$

The dielectric function $\varepsilon(q,\omega)$ can be written as

$$\varepsilon(q,\omega) = \varepsilon_\infty\frac{\omega_{LO}^2-\omega^2}{\omega_{TO}^2-\omega^2} + 4\pi\chi_{LM}. \tag{5}$$

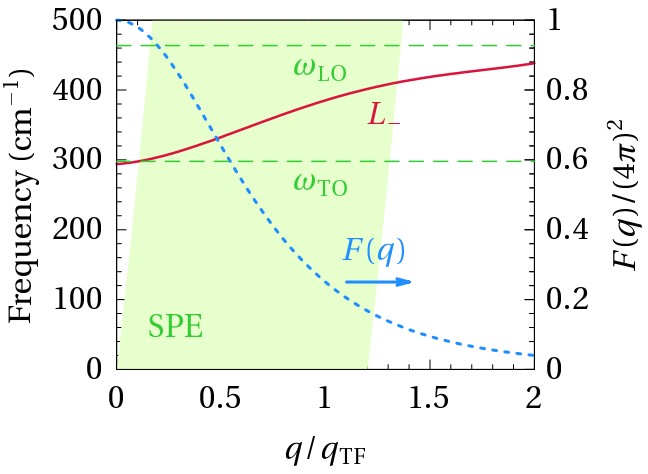


FIG. 3. Frequencies of the $L_-$ branch of the phonon-plasmon coupled mode at increasingly large values of wave vector. The single-particle excitation (SPE) region is shown as a shaded green area. The weighting function $F(q)$ [see Eq. (3)] is also plotted as a dotted line for reference.

Here, $\chi_{\mathrm{LM}}$ is the plasmon contribution to the electron gas susceptibility, which is calculated using the Lindhard-Mermin formalism:

$$\chi_{\mathrm{LM}}(q,\omega) = \frac{(1+\mathrm{i}\Gamma/\omega)[\chi_{\mathrm{L}}(q,\omega+\mathrm{i}\Gamma)]}{1+(\mathrm{i}\Gamma/\omega)[\chi_{\mathrm{L}}(q,\omega+\mathrm{i}\Gamma)/\chi_{\mathrm{L}}(q,0)]}, \tag{6}$$

with $\chi_{\mathrm{L}}$ given by the Lindhard integral

$$\chi_{\mathrm{L}}(q,\omega) = \frac{1}{2}\left(\frac{e}{q\pi}\right)^2 \int_0^\infty dk\, k^2 n_{\mathrm{BE}}[E(k),T] \int_0^\pi d\theta \sin\theta \times \left\{\frac{\Delta E+\hbar\omega-\mathrm{i}\hbar\Gamma}{(\Delta E+\hbar\omega)^2+(\hbar\Gamma)^2} + \frac{\Delta E-\hbar\omega+\mathrm{i}\hbar\Gamma}{(\Delta E-\hbar\omega)^2+(\hbar\Gamma)^2}\right\}, \tag{7}$$

where $\Delta E = E(k+q)-E(k)$, with $E(k)$ the nonparabolic band given by Eq. (2). As can be seen from Fig. 3, the wave vectors entering in the average of Eq. (3) lie within the Landau damping region. Therefore, it is imperative to use the Lindhard-Mermin approach to calculate the plasma response taking into account the overdamped nature of the plasma. It should be noted that the line shape Eq. (4) critically depends on the exact cancellation by the prefactor of the pole on the real axis of $\varepsilon(\omega,q)$. Irmer *et al.* [27] derived a different prefactor for the scattering efficiency that included phonon damping using a small-$q$ limit, Drude-type susceptibility. That expression breaks down the cancellation of the pole and it generates a spurious strong peak at the TO frequency when used with the Lindhard-Mermin susceptibility [22]. Since the damping constant of the plasma obtained from the Hall measurement data ($\Gamma \sim 420\,\mathrm{cm}^{-1}$) is much larger than the damping constant of the phonons, we neglect phonon damping in the model to avoid

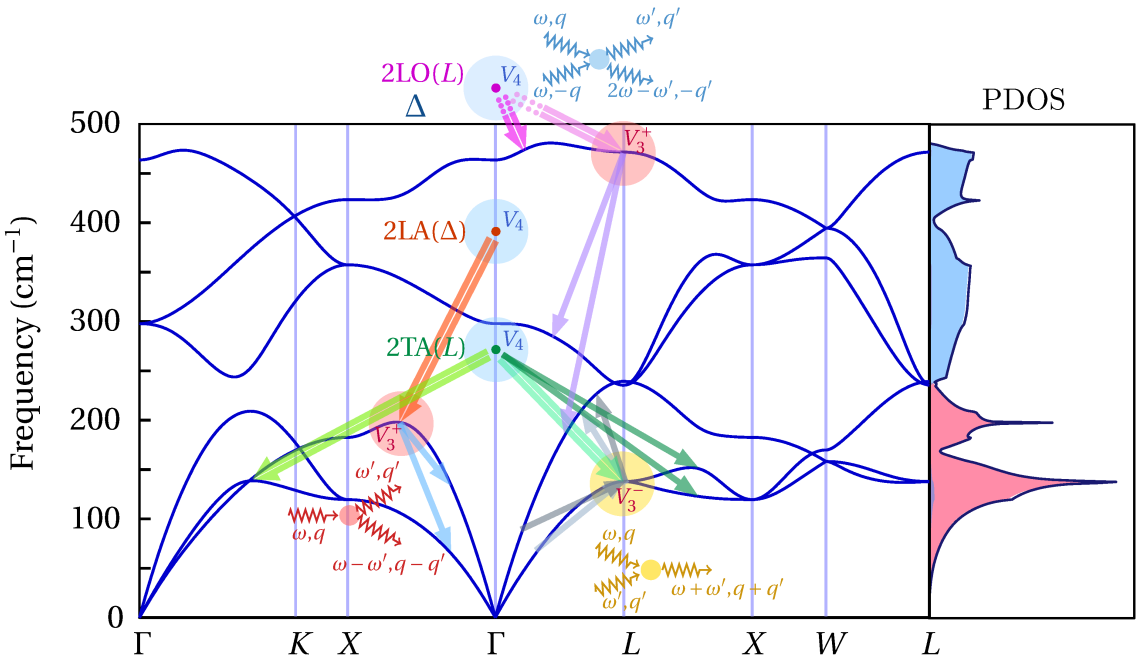


FIG. 4. Phonon dispersion of CdO along the main high-symmetry directions and the corresponding PDOS. The frequency axis has been scaled to bring the main critical points into accord with the sharp peaks observed in the second-order Raman spectrum. In the PDOS, the shaded blue (red) areas correspond to O (Cd) atomic motion. Arrows indicate the main paths for the anharmonic processes considered, namely cubic-anharmonicity decay and upconversion (red and yellow circles, respectively) and quartic-anharmonicity recombination(blue circles).

these inconsistency problems. As can be seen in Fig. 3, the low-energy branch of the coupled mode ($L_-$) shifts to higher energies for increasing wave vector, from slightly below $\omega_{\mathrm{TO}}$ to frequencies approaching $\omega_{\mathrm{LO}}$ at high $q$. Then, the weighted average Eq. (3) yields a broad band spanning the spectral region between TO and LO frequencies. The result of the calculation is shown in Fig. 1 as the light blue curve labeled CDF. Adding the CDF contribution to the OTD we obtain the green curve, which reproduces the overall shape and the main distinguishing features of the second-order Raman spectrum (see dashed and dotted vertical lines in Fig. 1). Only the weak shoulders at $X$ and $W$ in the acoustic range and a sharp peak at $X$ in the optical region lack its reflection into the Raman spectrum, probably due to small Raman susceptibility of the modes involved.

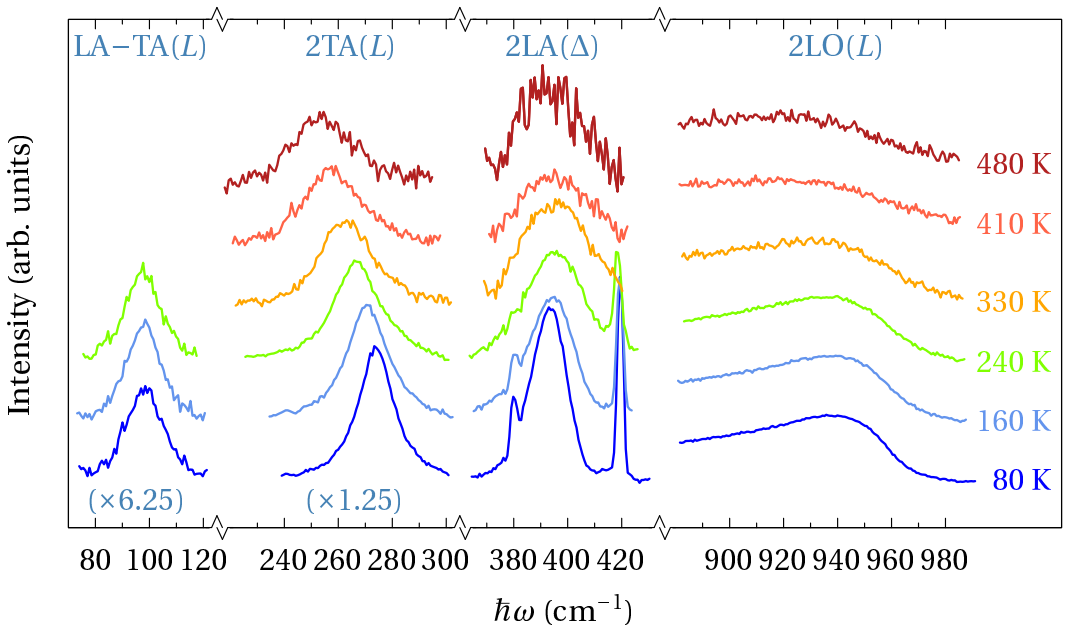


FIG. 5. Temperature dependence of the narrow second-order Raman features of CdO and the high-frequency cutoff at the 2LO($L$) overtone.

### D. Temperature dependence

Once a reliable scaled phonon dispersion has been established by comparison with the second-order Raman spectrum, we can use it to analyze the temperature dependence of the Raman peaks and the anharmonic phonon decay paths. The scaled phonon dispersion is plotted along the main high-symmetry directions in Fig. 4. Phonon lifetimes at zone center are commonly determined from the Raman spectra line widths, and the temperature dependence of the Raman line shape yields information about the anharmonic phonon decay processes [28, 29]. In the case of CdO, the temperature dependence of the narrow peaks observed in the second-order Raman spectra, which were identified as overtones at $L$ and $\Delta$ critical points, can probe the anharmonicity of the phonons involved. Figure 5 shows the Raman spectra at temperatures in the 80 – 480 K range after removing the background, which for the 2TA and 2LA region is, as previously discussed, mainly due to overdamped plasmon excitations. The temperature dependence is quite different for the different modes. As expected, the LA−TA difference mode changes very little with temperature, because of the cancellation of thermal expansion effects and the lack of effective decay channels. Unfortunately, the intensity of this peak is extremely weak and can hardly be observed at higher temperatures. In contrast, the 2TA($L$) peak

manifestly broadens and shifts to lower frequencies as the temperature increases from 80 to 480 K, whereas the 2LA($\Delta$) peak steadily broadens but its frequency slightly increases with temperature. In a similar fashion, the high-frequency cut-off at the 2LO($L$) overtone is smoothed out with increasing temperature but its frequency practically remains unaltered. To explain the temperature dependence of the second-order Raman spectrum of CdO, next we consider the effects of lattice thermal expansion and anharmonicity on the phonon modes.

*1. Lattice thermal expansion*

The thermal expansion coefficient in a cubic crystal is given by

$$\alpha = \frac{\gamma c_{\mathrm{V}}}{3B}, \tag{8}$$

where $\gamma$ is the average Grüneisen parameter, $c_{\mathrm{V}}$ is the specific heat, and $B = -V(\partial P/\partial V)_T$ is the bulk modulus. In terms of the mode contribution to the specific heat $c_{\mathrm{V}s}(q) = (\hbar\omega_{qs}/V)\,\partial n_{\mathrm{BE}}(\omega_{qs}, T)/\partial T$ and the mode Grüneisen parameter $\gamma_{qs} = -(V/\omega_{qs})\,\partial\omega_{qs}/\partial V$, the average Grüneisen parameter is

$$\gamma = \frac{\sum\limits_{qs} \gamma_{qs} c_{\mathrm{V}s}(q)}{\sum\limits_{qs} c_{\mathrm{V}s}(q)}, \tag{9}$$

and the specific heat can be written as

$$c_{\mathrm{V}} = \frac{k_{\mathrm{B}}}{V} \sum_{qs} \left(\frac{\hbar\omega_{qs}}{2k_{\mathrm{B}}T}\right)^2 \frac{1}{\sinh^2\left(\dfrac{\hbar\omega_{qs}}{2k_{\mathrm{B}}T}\right)}. \tag{10}$$

All the above quantities can be calculated from the corrected phonon dispersion obtained from DFPT. We evaluate the sums over the Brillouin zone using the set of 10 special reciprocal-space points derived by Chadi and Cohen [30]. At 300 K we obtain $\alpha = 1.36 \times 10^5$ K$^{-1}$ and $c_{\mathrm{V}} =$ 43.3 J/mol K, in excellent agreement with recent data for CdO ($\alpha = 1.4 \times 10^5$ K$^{-1}$ and $c_{\mathrm{V}} = 43.6$ J/mol K) [31]. In the quasiharmonic approximation, the phonon shift due to thermal expansion of the lattice $\Delta_0$ is obtained from

$$\Delta_0 = -\omega_0 \int_0^T 3\gamma\alpha(T')\,dT' \tag{11}$$

MOCVD CdO layers grown on $r$-plane sapphire are fully relaxed, with perpendicular and *in-plane* lattice parameters in agreement with the bulk value [13]. Consequently, we assume that the relatively thick layer studied here is effectively decoupled from the sapphire substrate and the effects of differential expansion can be neglected.

*2. Anharmonic decay*

Anharmonic interactions couple the harmonic eigenstates and induce a complex phonon self-energy $\Pi(\omega) = \Delta(\omega) + i\Gamma(\omega)$ which accounts for the finite lifetime of the phonons. The imaginary part of the self-energy yields the Raman line shape broadening, which has an associated frequency shift due to the real part of the phonon self-energy [32]. Second-order Stokes Raman scattering in CdO involves the creation of a two-phonon state in a single event. The lifetime of such excited state is limited by the anharmonic decay of each constituent phonon (three-phonon processes) as well as by the recombination of the two-phonon state via quartic anharmonicity resulting in pairs of lower lying phonons with opposite wave-vectors (four-phonon processes). The decay rate of the two-phonon state is then $\tau^{-1} = \tau^{-1}_{(3),1} + \tau^{-1}_{(3),2} + \tau^{-1}_{(4),1\oplus 2}$, where $\tau^{-1}_{(3),i}$ is the cubic-anharmonicity decay rate of phonon $i$ and $\tau^{-1}_{(4),1\oplus 2}$ is the recombination rate of the two-phonon state via quartic anharmonicity. Most of the observed Raman features correspond to overtones of acoustic modes, which generally exhibit longer lifetimes than optical modes due to the low density of phonon states available for decay. Thus, quartic-anharmonicity interactions have to be included to explain the temperature dependence measured in the experiments.

A perturbative analysis of the anharmonic interactions was first applied to group-IV semiconductors [28] and later extended to a number of compound semiconductors [33–37]. Assuming that the Bose-Einstein factors and the anharmonic potentials vary slowly around the considered phonon frequencies, the imaginary part of the phonon self-energy for cubic anharmonicity can be written to the lowest order in perturbation theory as

$$\Gamma^{(3)}(\omega, T) = |V_3^+|^2(1 + n_1 + n_2)\rho^+(\omega) + |V_3^-|^2(n_1 - n_2)\rho^-(\omega), \tag{12}$$

where $\rho^+(\omega)$ and $\rho^-(\omega)$ are, respectively, the two-phonon sum and difference density of states, $n_1$ and $n_2$ are the Bose-Einstein occupation factors for the phonon products, and $V_3^+$ and $V_3^-$ are effective cubic-anharmonicity potentials. The second term corresponds to an upconversion process in which a phonon $\omega_1$ is annihilated and a higher energy phonon $\omega_2$ is created. The real part of the phonon self-energy can be obtained from a Kramers-Kronig transformation. In addition, there is a purely real contribution to the self-energy arising from quasi-elastic scattering with pairs of opposite wave-vector phonons. This contribution, which is associated with a first-order loop diagram and is referred to as 4-phonon scattering, is particularly important in laminar crystals exhibiting low-lying optical branches [29]. In the case of CdO, the PDOS

maximum occurs at a sharp peak at $\sim 140$ cm$^{-1}$, which may enable a relevant contribution of the 4-phonon scattering mechanism.

The relatively weak cubic-anharmonicity decay of the acoustic modes is not sufficient to explain the observed variation of the second-order Raman peaks with temperature. Quartic anharmonicity, which gives rise to four-phonon processes, has shown to be important in many cases [38, 39]. Balkanski *et al.* [38] gave explicit expressions for the quartic-anharmonicity contributions to the self-energy. To estimate the overtone recombination rate $\tau^{-1}_{(4),1\oplus 2}$, we consider the quartic interaction corresponding to the annihilation of phonon $\omega_1$ and creation of phonon s $\omega_2$ and $\omega_3$ [38], with $\omega_1$ fixed at the half-frequency of the overtone. Under the same assumptions leading to Eq. (12), the contribution of four-phonon recombination of the overtone can be approximated by

$$\Gamma^{(4)}(\omega, T) = 3|V_4|^2\{n_1(1+n_2)(1+n_3) - (1+n_1)n_2n_3\}\rho^+(\omega), \tag{13}$$

where $V_4$ is an effective quartic anharmonic potential. Note that here $\omega$ stands for the frequency of the overtone. The main paths for phonon decay via cubic and quartic anharmonicity considered in our analysis are depicted in Fig. 4.

For small anharmonic shifts and broadenings compared to the harmonic frequency, the Raman scattering line shape is [28]

$$I(\omega) \propto \frac{\Gamma(\omega)}{[\omega_0 + \Delta_0 + \Delta(\omega) - \omega]^2 + \Gamma(\omega)^2}, \tag{14}$$

which yields the frequency and line width of the renormalized phonon. Note that for a slowly varying self-energy, the line shape is Lorentzian-like with full width at half maximum (FWHM) equal to $2\Gamma(\omega)$. Next, we analyze the observed temperature dependence of each of the modes displayed in Fig. 5 in the light of the theoretical framework described above.

### *3. 2TA(L)*

The 2TA($L$) peak exhibits a typical temperature dependence with a steady broadening and frequency downshift as temperature increases. We identify representative frequencies for cubic-anharmonicity decay of the TA($L$) mode along the $\Gamma$–$L$ line. Only upconversion processes are possible (gray pointing-up arrows in Fig. 4), with average frequencies $\omega_1 = 79$ cm$^{-1}$

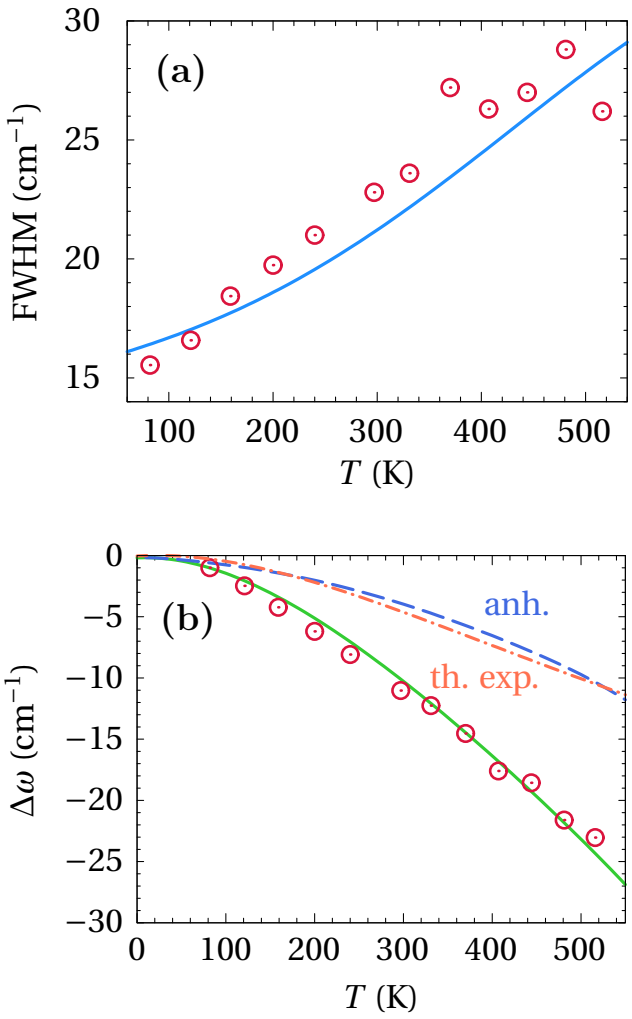


FIG. 6. (a) Temperature dependence of the full width at half maximum (FWHM) of the 2TA($L$) peak (circles) and the FWHM calculated using the anharmonic decay model (solid line). (b) Thermal downshift of the 2TA($L$) frequency (circles) and the calculated contributions of anharmonic decay (dashed line) and lattice thermal expansion (dashed-dotted line). The solid green line is the sum of anharmonic decay and lattice expansion contributions.

and $\omega_2 = 217.5$ cm$^{-1}$. Quartic-anharmonicity recombination of the two-phonon state can proceed via creation of pairs of opposite wave-vector phonons at $L$ or at the $\Gamma$–$K$ and $L$–$X$ lines, as indicated by the green arrows in Fig. 4. Figure 6(a) shows the FWHM of the 2TA($L$) peak measured for temperatures from 80 to 510 K. The FWHM were determined from Lorentzian fits to the spectra and the error bars correspond to the asymptotic standard errors of the fit. The anharmonic model based on Eqs. (12) and (13) reproduce well the experimental results. Table I lists the values of the effective anharmonic potentials that were used to obtain a best

TABLE I. Cubic ($V_3^{+,-}$) and quartic ($V_4$, $V_{4ps}$) anharmonicity effective potentials used to describe our data, and anharmonicity-limited phonon lifetimes at 80 and 300 K. $\Gamma_b$ is the constant background contribution to the FWHM that accounts for background impurity scattering and inhomogeneous broadening.

| Mode | $\lvert V_3^+\rvert^2$ | $\lvert V_3^-\rvert^2$ | $\lvert V_4\rvert^2$ | $V_{4ps}$ | $\tau_{anh}^{80K}$ | $\tau_{anh}^{300K}$ | $\Gamma_b$ |
|---|---|---|---|---|---|---|---|
| | ($cm^{-2}$) | ($cm^{-2}$) | ($cm^{-1}$) | ($cm^{-1}$) | (ps) | (ps) | ($cm^{-1}$) |
| TA-LA($L$) | 10 | 10 | 10 | | 9.5 | 2.1 | 15.0 |
| 2TA($L$) | | 5.5 | 5.7 | −0.1 | 6.8 | 0.9 | 15.6 |
| 2LA($\Delta$) | 22 | | 15 | 1 | 2.5 | 0.5 | 12.0 |
| 2LO($L$) | 26 | | 25 | 0.8 | 0.6 | 0.3 | |

fit to the data, as well as the constant background contribution which accounts for impurity scattering and the inhomogeneous broadening caused by the finite width of the peak in the PDOS. The variation of FWHM with temperature allows us to estimate the anharmonic-decay limited phonon lifetime $\tau_{anh}$ from FWHM $= \hbar(\tau_{anh}^{-1} + \tau_b^{-1})$, where $\tau_b^{-1}$ accounts for the phonon broadening by background impurities and inhomogeneous broadening, and $\hbar = 5.3089 \times 10^{-12}$ $cm^{-1}$s. Values of $\tau_{anh}$ and $\tau_{anh}$ at 80 and 300 K are also listed in Table I. In Fig. 6(b) we analyze the frequency downshift with temperature, which is well described by the sum of the thermal expansion contribution (dashed doted line) and the anharmonic shift (dashed line). Only a marginal contribution of the 4-phonon scattering ($V_{4ps} = -0.1$ $cm^{-1}$) was included to finely match the model with the experimental results (solid green line).

*4. 2LA(Δ)*

The temperature dependence of the 2LA(Δ) mode is quite different from that of the 2TA($L$) mode. As can be seen from the spectra in Fig. 5, whereas the line width increases with temperature at a significantly higher rate than that of the 2TA($L$) mode, the 2LA(Δ) mode frequency shows a small upshift with temperature. The LA(Δ) mode can decay into a pair of transverse and longitudinal acoustic phonons on the Γ–$X$ line, with representative frequencies $\omega_1 = 62$ $cm^{-1}$ and $\omega_2 = 135$ $cm^{-1}$, as depicted by the cyan arrows in Fig. 4. Recombination of the two-phonon state results in pairs of opposite wave-vector LA phonons on the Γ–$X$ line (orange arrows in Fig. 4). Figure 7(a) displays the temperature dependence of the FWHM of the 2LA(Δ) mode

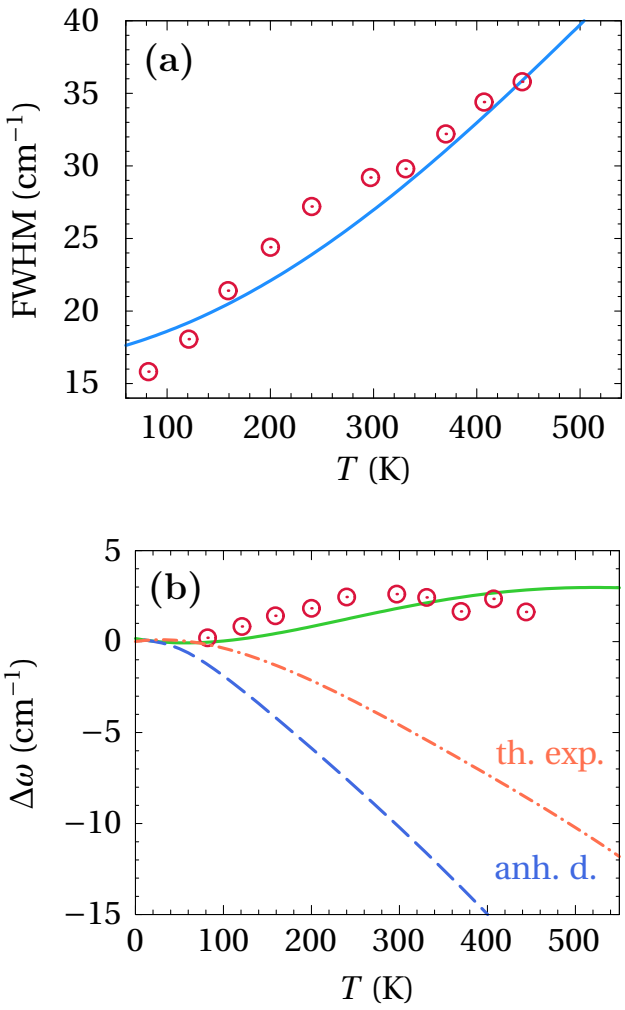


FIG. 7. (a) Temperature dependence of the full width at half maximum (FWHM) of the 2LA(Δ) peak (circles) and the FWHM calculated using the anharmonic decay model (solid line). (b) Thermal downshift of the 2LA(Δ) frequency (circles) and the calculated contributions of anharmonic decay (dashed line), 4-phonon scattering (dotted line), and lattice thermal expansion (dashed-dotted line). The solid green line is the sum of anharmonic decay, 4-phonon scattering, and lattice expansion contributions.

(circles), which is well reproduced by the anharmonic model (for the model parameters, see Table I). The phonon shift associated with the real part of the phonon self-energy is plotted as a dashed line in Fig. 7(b). The anharmonic decay yields a negative frequency shift of comparable magnitude to the thermal expansion downshift (dashed-doted line). A substantial contribution of the 4-phonon scattering has to be included to achieve good agreement with the experimental frequencies. The model reproduces well the observed saturation of the frequency upshift at higher temperatures.

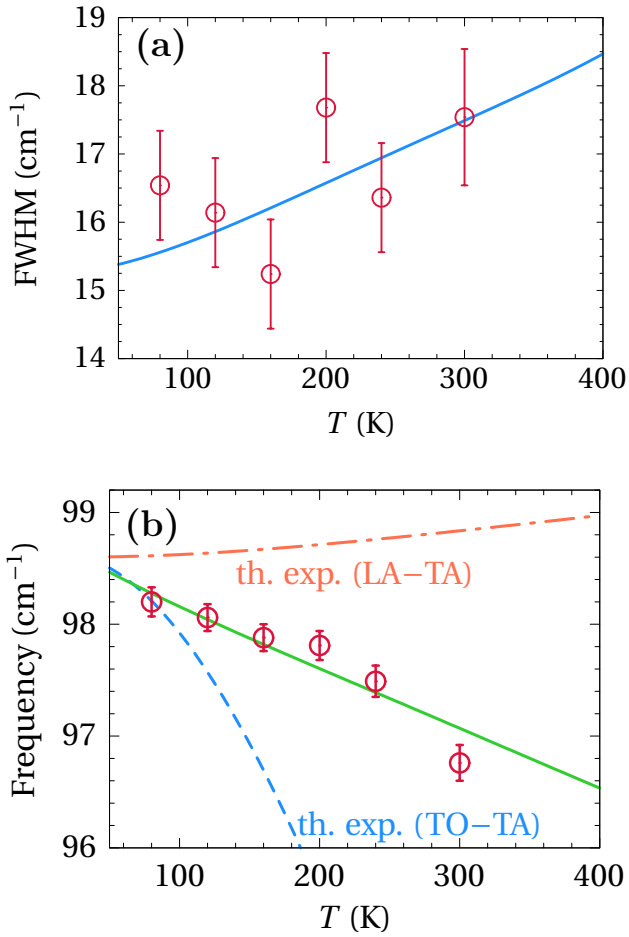


FIG. 8. (a) Temperature dependence of the full width at half maximum (FWHM) of the LA−TA($L$) peak (circles) and the FWHM calculated using the anharmonic decay model (solid line). (b) Thermal downshift of the LA-TA($L$) frequency (circles) and the calculated contributions of lattice thermal expansion for LA−TA($L$) (dashed-dotted line) and TO−TA($L$) . The solid green line is the sum of the anharmonic decay and the lattice expansion contribution for LA−TA($L$).

*5. LA−TA(L)*

For completeness, we also discuss the LA−TA($L$) difference mode. Unfortunately, this is an extremely weak peak and it becomes buried in the background of the spectra at temperatures higher than 300 K, so only a limited range of temperatures is available and the results should be taken as qualitative. Being a difference mode, we expect the anharmonic effects to be small. First, it has a small frequency, so the PDOS available for decay is very small. Second, the lattice expansion effects should tend to cancel for the difference mode. Only upconversion processes are possible for the TA($L$) mode, which are indicated by pointing-up arrows in Fig. 4.

The LA($L$) mode can decay into phonons of the LA and TA branches in the $\Gamma$-$L$ line at frequencies of 122 and 119 cm$^{-1}$, respectively (this path has been omitted in Fig. 4 to avoid cluttering the figure). Figure 8(a) shows the FWHM of the difference mode measured for temperatures up to 300 K, compared with the theoretical model. Generic nominal anharmonic potentials $|V_3^+|^2 = |V_3^-|^2 = |V_4|^2 = 10$ cm$^{-2}$ were used in the calculations because the quality of the data does not allow refining the estimates. The corresponding real part of the phonon self-energy yields a small negative shift in this temperature range. Since at the $L$ point the frequencies of the LA and TO modes are almost identical (see Fig. 4), one might also consider TO−TA as a possible assignment for this mode. However, we find that the Grüneisen parameters for the TO and LA modes differ considerably ($\gamma_{\mathrm{TO}} = 4.93$ vs. $\gamma_{\mathrm{LA}} = 1.16$). This means that the thermal expansion shift of TO−TA [dashed line in Fig. 8(b)] would play a dominant role in its temperature dependence, which is not observed in the experiment. This would suggest that this mode is mainly a difference mode of acoustic branches primarily involving Cd motion.

*6. The 2LO(L) cutoff*

Unlike the second-order modes previously analyzed, the 2LO($L$) mode does not appear as a sharp peak in the Raman spectrum but it marks an abrupt high-frequency cutoff. As can be seen in Fig. 5, this step-like cutoff broadens and slightly downshifts as temperature increases. To extract more quantitative information from the spectra, we have modeled the high-frequency cutoff using a generalized sigmoidal curve

$$\sigma(\omega) = \frac{A}{\left[1 + \exp[B(\omega - \omega_0)]\right]^{1/2}}, \tag{15}$$

where $A$, $B$, and $\omega_0$ are fitting parameters. To reduce the degrees of freedom, the exponent in the denominator is kept fixed at 1/2, as this value yields similarly good fits for all the spectra. The physically relevant parameters of the fit are the midpoint $\omega_0$ and the slope at midpoint $-2^{-5/2}AB$, which are related to the frequency and FWHM of the 2LO($L$) mode.

To determine this relationship, we have fitted the sigmoidal curve Eq. (15) to the convolution of a Lorentzian function with the PDOS with a doubled frequency axis. One should bear in mind that this procedure may introduce an artificial inhomogeneous broadening if the scattering efficiency of the 2LO mode along the $\Gamma$-$L$ line, responsible for the high-frequency tail in the PDOS, is lower than at the $L$ point. The changes in slope and midpoint of the convolved

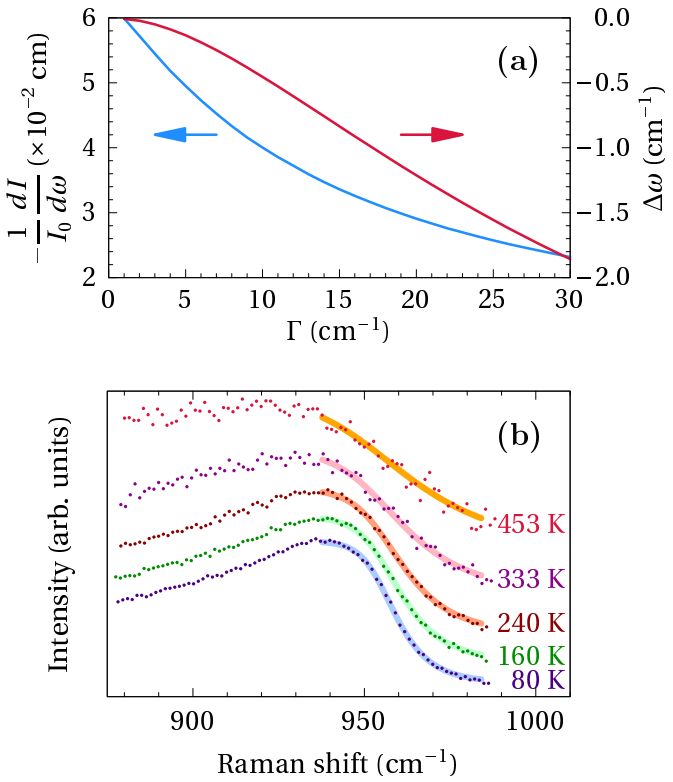


FIG. 9. (a) Slope of the sigmoidal function at midpoint (blue curve, left axis) and the shift of the midpoint (red curve, right axis) as a function of the FWHM of the Lorentzian line shape. (b) Fits of the sigmoidal function (solid lines) to the experimental data (points) at different temperatures.

step-like structure are plotted in Fig. 9(a), which shows that the slope gradually decreases as the Lorentzian line width increases, and the midpoint shifts to lower frequencies. By fitting the sigmoidal curve to the Raman spectrum as displayed in Fig. 9(b) and using the calibration provided in Fig. 9(a), we can extract the values of the FWHM for the 2LO($L$) mode. These are plotted as a function of temperature in Fig. 10(a).

Representative frequencies for decay of the LO($L$) mode are identified on the TO and LA branches along the Γ-$L$ line as depicted in Fig. 4 by purple arrows. Quartic-anharmonicity recombination paths are depicted by magenta discontinuous arrows. The increase of the FWHM with temperature is well reproduced by the anharmonic model with the parameters listed in Table I. Note that the the magnitude of the FWHM is fairly low, and that no background contribution had to be added. This is consequence of the inhomogeneous broadening associated with the convolution as discussed above. After correcting for the shift of the sigmoidal curve [see Fig. 9(a)], the frequency of the 2LO($L$) mode does not change significantly for temperatures

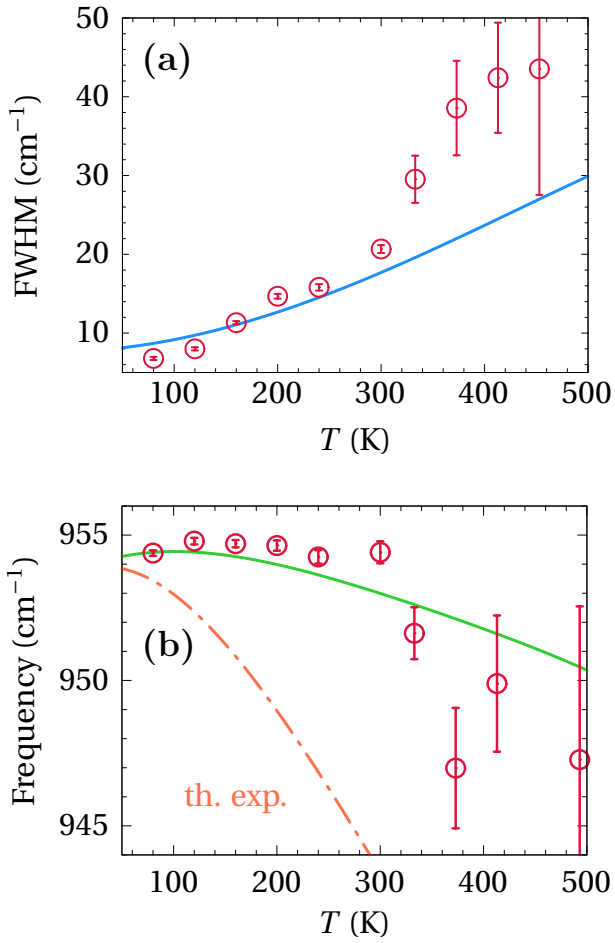


FIG. 10. (a) FWHM of the 2LO($L$) mode extracted from the second-order spectra high-frequency cutoff (circles). The solid line is a calculation using the anharmonic model. (b) Shift of the second-order spectra cutoff frequency with increasing temperature (circles). The dashed-dotted line is the contribution of the lattice thermal expansion. The green solid line is the sum of the anharmonic decay, 4-phonon scattering and thermal expansion contributions.

up to 300 K, as can be seen in Fig. 10(b), indicating that in this case 4-phonon scattering also tends to compensate the effect of the lattice thermal expansion. At higher temperatures the high-frequency cutoff seems to downshift slightly, but the spectra become very weak and noisy making the analysis uncertain in this higher temperature range.

## IV. CONCLUSIONS

We have performed a comprehensive study of Raman scattering of rock-salt CdO. Despite first-order Raman scattering being forbidden by the symmetry of the lattice, the second-order Raman spectra can still yield a good deal of information. The particular phonon dispersion of CdO contains sharp van-Hove singularities that result in narrow peaks in the second-order spectra which can be readily identified from *ab initio* calculations. Although presently DFPT calculations substantially underestimate the phonon frequencies of CdO, we can exploit these hallmarks in the spectra to correct the calculated phonon dispersion and PDOS for subsequent use in the modeling of anharmonic interactions.

The second-order Raman spectrum is primarily an overtone spectrum, as indicated by the good agreement that is observed with the PDOS with the frequency axis doubled, except for a wide, intense central band that is not correlated with the PDOS. We attribute this band to Raman scattering by large-wave-vector coupled-plasmon excitations of the overdamped plasma present in the $n$-type sample. A detailed calculation of this contribution using the Lindhard-Mermin formalism yields an excellent agreement with the experimental data, thus supporting this assignment.

The temperature dependence of the second-order peaks has been analyzed using a semi-empirical anharmonic decay model based on the phonon self-energy that includes phonon decay via cubic- and quartic-anharmonicity interactions and quasi-elastic scattering with low-frequency modes (4-phonon scattering mechanism). The cubic-anharmonicity decay is relatively weak for the acoustic modes and quartic-anharmonicity interactions have to be included to explain the experimental results. While the 2TA($L$) mode exhibits a typical temperature behavior with a frequency downshift linked with the line broadening, the 2LA($\Delta$) shows a slight blueshift associated with the 4-phonon scattering mechanism that compensates the thermal expansion shift. A similar behavior is observed for the high-frequency cutoff of the second Raman spectrum delimited by the 2LO($L$) frequency.

### ACKNOWLEDGMENTS

This work was partially funded by the Spanish Ministry of Economy, Industry and Competitiveness (MINECO) under Project PID2020-114796RB-C22, and the Generalitat Valenciana un-

der project PROMETEU/2021/066. Javier Yeste holds a FPU (Formacion de Professorat Universitari) predoctoral contract from the Spanish Ministry of Science, Innovation and Universities (MICIU) that he wants to thank.

---

[1] J. A. Spencer, A. L. Mock, A. G. Jacobs, M. Schubert, Y. Zhang, and M. J. Tadjer, Appl. Phys. Rev. **9**, 011315 (2022).

[2] K. M. Yu, M. A. Mayer, D. T. Speaks, H. He, R. Zhao, L. Hsu, S. S. Mao, E. E. Haller, and W. Walukiewicz, J. Appl. Phys. **111**, 123505 (2012).

[3] L. Li, S. Liang, S. Li, J. Wang, S. Wang, G. Dong, and G. Fu, Nanotechnology **25**, 425402 (2014).

[4] E. Sachet, C. T. Shelton, J. S. Harris, B. E. Gaddy, D. L. Irving, S. Curtarolo, B. F. Donovan, P. E. Hopkins, P. A. Sharma, A. L. Sharma, et al., Nature Mat. **14**, 414 (2015).

[5] J. A. Tomko, E. L. Runnerstrom, Y.-S. Wang, W. Chu, J. R. Nolen, D. H. Olson, K. P. Kelley, A. Cleri, J. Nordlander, J. D. Caldwell, et al., Nat. Nanotechnol. **16**, 47 (2020).

[6] P. H. Jefferson, S. A. Hatfield, T. D. Veal, P. D. C. King, C. F. McConville, J. Zúñiga–Pérez, and V. Muñoz–Sanjosé, Appl. Phys. Lett. **92**, 022101 (2008).

[7] J. Tamayo-Arriola, E. M. Castellano, M. M. Bajo, A. Huerta-Barberà, E. Muñoz, V. Muñoz-Sanjosé, and A. Hierro, ACS Photonics **6**, 2816 (2019).

[8] B. Luo, Y. Yao, E. Tian, H. Song, X. Wang, G. Li, K. Xi, B. Li, H. Song, and L. Li, Proc. Natl. Acad. Sci. U.S.A. **116**, 17213 (2019).

[9] F. P. Koffyberg, Phys. Rev. B **13**, 4470 (1976).

[10] L. Lindsay and D. S. Parker, Phys. Rev. B **92** (2015).

[11] G. Schaack and N. Uhle, Solid State Commun. **19**, 315 (1976).

[12] J. E. Potts, C. T. Walker, and I. R. Nair, Phys. Rev. B **8**, 2756 (1973).

[13] J. Zuñiga-Pérez, C. Munuera, C. Ocal, and V. Muñoz-Sanjosé, J. Cryst. Growth **271**, 223 (2004).

[14] R. Cuscó, J. Ibánez, N. Domènech-Amador, L. Artús, J. Zúñiga Pérez, and V. Muñoz Sanjose, J. Appl. Phys. **107**, 063519 (2010).

[15] R. Oliva, J. Ibáñez, L. Artús, R. Cuscó, J. Zúñiga Pérez, and V. Muñoz Sanjosé, J. Appl. Phys. **113**, 053514 (2013).

[16] P.-F. Lory, S. Pailhès, V. M. Giordano, H. Euchner, H. D. Nguyen, R. Ramlau, H. Borrmann, M. Schmidt, M. Baitinger, M. Ikeda, et al., Nat. Commun. **8**, 491 (2017).

[17] ABINIT is a common project of the Université Catholique de Louvain, Corning Incorporated, and other contributors (http://www.abinit.org). X. Gonze, J.-M. Beuken, R. Caracas, F. Detraux, M. Fuchs, G.-M. Rignanese, L. Sindic, M. Verstraete, G. Zerah, F. Jollet, et al., Comput. Mater. Sci. **25**, 478 (2002).

[18] K. F. Garrity, J. W. Bennett, K. M. Rabe, and D. Vanderbilt, Comput. Mater. Sci. **81**, 446 (2014).

[19] M. Cardona and G. Güntherodt, eds., *Light Scattering in Solids II*, vol. 50 of *Topics Appl. Phys.* (Springer Berlin Heidelberg, 1982).

[20] *Rutgers University, Open-source pseudopotential library*, URL `http://physics.rutgers.edu/gbrv`.

[21] B. A. Weinstein and M. Cardona, Phys. Rev. B **7**, 2545 (1973).

[22] M. Ramsteiner, O. Brandt, and K. H. Ploog, Phys Rev B **58**, 1118 (1998).

[23] J. Tamayo-Arriola, A. Huerta-Barberà, M. M. Bajo, E. Muñoz, V. Muñoz-Sanjosé, and A. Hierro, Appl. Phys. Lett. **113**, 222101 (2018).

[24] R. Cuscó, E. Alarcón-Lladó, J. Ibáñez, T. Yamaguchi, Y. Nanishi, and L. Artus, J. Phys. Cond. Mat. **21**, 415801 (2009).

[25] D. Olego and M. Cardona, Phys. Rev. B **24**, 7217 (1981).

[26] M. Cardona and G. Güntherodt, eds., *Light Scattering in Solids IV*, vol. 54 of *Topics Appl. Phys.* (Springer Berlin, 1984).

[27] G. Irmer, V. V. Toporov, B. H. Bairamov, and J. Monecke, Phys. Status Solidi B **119**, 595 (1983).

[28] J. Menéndez and M. Cardona, Phys. Rev. B **29**, 2051 (1984).

[29] R. Cuscó, B. Gil, G. Cassabois, and L. Artús, Phys. Rev. B **94**, 155435 (2016).

[30] D. J. Chadi and M. L. Cohen, Phys. Rev. B **8**, 5747 (1973).

[31] *AzoMaterials*, URL `http://www.azom.com/article.aspx?ArticleID=8422`.

[32] R. A. Cowley, Rep. Prog. Phys. **31**, 123 (1968).

[33] A. Göbel, T. Ruf, C.-T. Lin, M. Cardona, J.-C. Merle, and M. Joucla, Phys. Rev. B **56**, 210 (1997).

[34] J. Serrano, F. J. Manjón, A. H. Romero, F. Widulle, R. Lauck, and M. Cardona, Phys. Rev. Lett. **90** (2003).

[35] R. Cuscó, E. Alarcón-Lladó, J. Ibáñez, L. Artús, J. Jiménez, B. Wang, and M. J. Callahan, Phys. Rev. B **75**, 165202 (2007).

[36] N. Domènech-Amador, R. Cuscó, L. Artús, T. Yamaguchi, and Y. Nanishi, Phys. Rev. B **83**, 245203 (2011).

[37] R. Cuscó, N. Domènech-Amador, S. Novikov, C. T. Foxon, and L. Artús, Phys. Rev. B **92**, 075206 (2015).

[38] M. Balkanski, R. F. Wallis, and E. Haro, Phys. Rev. B **28**, 1928 (1983).

[39] X. Yang, T. Feng, J. S. Kang, Y. Hu, J. Li, and X. Ruan, Phys. Rev. B **101**, 161202 (R) (2020).